JOURNAL OF APPLIED CRYSTALLOGRAPHY

ISSN 1600-5767

Received 14 May 2017
Accepted 7 July 2017

Edited by V. Holý, Charles University, Prague, Czech Republic

Keywords: X-ray dynamical diffraction theory; reciprocal space maps; transversely restricted wavefronts; instrumental functions.

Applications of dynamical theory of X-ray diffraction by perfect crystals to reciprocal space mapping

Vasily I. Punegov,[a,b]* Konstantin M. Pavlov,[c,d] Andrey V. Karpov[a] and Nikolai N. Faleev[e]

[a]Komi Research Center, Ural Division, Russian Academy of Sciences, Syktyvkar, 167982, Russian Federation, [b]Syktyvkar State University, Syktyvkar, 167001, Russian Federation, [c]School of Science and Technology, University of New England, NSW 2351, Australia, [d]School of Physics and Astronomy, Monash University, VIC 3800, Australia, and [e]Ira Fulton School, School of ECEE, Solar Power Laboratory, Arizona State University, 7700 South River Parkway, Tempe, AZ 85284, USA. *Correspondence e-mail: vpunegov@dm.komisc.ru

The classical dynamical theory of X-ray diffraction is expanded to the special case of transversely restricted wavefronts of the incident and reflected waves. This approach allows one to simulate the two-dimensional coherently scattered intensity distribution centred around a particular reciprocal lattice vector in the so-called triple-crystal diffraction scheme. The effect of the diffractometer's instrumental function on X-ray diffraction data was studied.

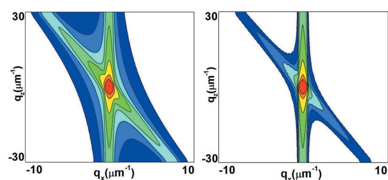

© 2017 International Union of Crystallography

1. Introduction

Recently, triple-crystal X-ray diffraction (Iida & Kohra, 1979; Zaumseil & Winter, 1982) has been successfully applied to investigate a variety of crystalline structures (Bhagavannarayana & Zaumseil, 1997; Kazimirov *et al.*, 1990; Faleev *et al.*, 2013; Lomov *et al.*, 2014; Punegov, 2015) and X-ray optical elements (Jergel *et al.*, 1999; Irzhak *et al.*, 2015). Despite the fact that diffracted waves contain both coherent and diffuse scattered components, typically only the latter, caused by scattering on defects, is analysed, often only qualitatively. However, if one wants to quantitatively analyse the scattered intensity distribution (*i.e.* reciprocal space map) near a particular reciprocal lattice vector where the coherent scattering is strong, some approximations of coherent scattering (Punegov, 2012) have to be used. These approximations are used because the current dynamical diffraction approach (Authier, 2001) assumes that the incident wave is a plane wave. Such an assumption results in the Dirac delta function intensity distribution (Kaganer *et al.*, 1997) for the coherent scattering component, which makes impossible quantitative analysis of a diffraction pattern near the particular reciprocal lattice vector (Fig. 1).

It should be noted that quantitative analysis of coherently scattered waves was recently performed for crystals having a finite length in the lateral direction (Punegov *et al.*, 2014, 2016; Pavlov *et al.*, 2017). In this case the limited lateral size of such crystals restricts the illuminated area and, therefore, the diffracted intensity distribution is not a Dirac delta function anymore.

The diffraction of transversely restricted X-ray beams was considered (Berenson, 1989; Bushuev, 1998; Bushuev & Oreshko, 2007) in the case of the so-called double-crystal diffraction scheme. In particular, an approach using Green

functions was employed by Bushuev (1998) and Bushuev & Oreshko (2007) to describe the spatially inhomogeneous Bragg diffraction by an ideal crystal. However, the results of Bushuev (1998) and Bushuev & Oreshko (2007) cannot be directly applied for the triple-crystal diffraction scheme because their approach integrates the angular distribution of the reflected wave, which can be resolved in the triple-crystal diffraction scheme because of the presence of the analyser crystal.

This paper aims to provide a quantitative analysis of two-dimensional diffraction intensity distributions of coherently scattered waves within the framework of dynamical diffraction theory in the case of transversely restricted wavefronts of the incident and diffracted waves.

2. Diffraction theory for transversely restricted X-ray waves

Let us consider dynamical X-ray diffraction by a perfect crystal in a Cartesian system of coordinates where the x and y axes are parallel to the top crystal surface, and the z axis is directed inside the crystal (Fig. 2). Thus, the xOz plane is the plane of diffraction. The angle between the wavevector of an incident monochromatic plane wave (of unit intensity) and the positive $\mathbf{x}$ direction is $\theta = \theta_B + \omega$, where ω is the angular deviation from the Bragg diffraction angle θ_B (Fig. 2). The entrance slit S_1 determines the wave's transverse width w. Thus, the illuminated area of the top surface of the crystal is $l_x^{(\rm in)} \simeq w/\sin\theta_B$. The transverse size of the reflected (scattered) wave is limited by the exit slit S_2, which defines a lateral size of $l_x^{(\rm ex)}$ (Fig. 2) at the crystal surface. We also assume that the propagation distance between the particular slit and the crystal surface is small enough to satisfy the geometrical optics approximation.

For the sake of simplicity, we consider a symmetrical diffraction case in Bragg geometry (Fig. 2). The dynamical diffraction by an ideal crystal can be described by Takagi's equations (Takagi, 1962) as follows:

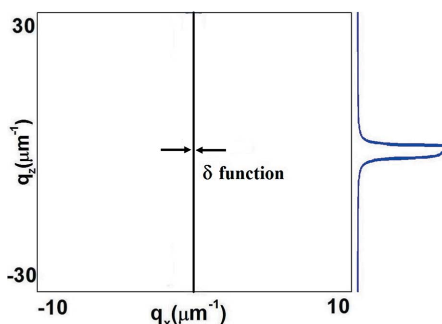

Figure 1
Reciprocal space map of diffracted intensity distribution near the 111 reflection of a semi-infinite Si perfect crystal in the case on an incident plane wave. The intensity distribution along the q_x direction is described by a Dirac δ function, while the intensity distribution along the q_z direction (blue curve), *i.e.* along the diffraction vector, is the well recognized Darwin curve.

$$\begin{cases} \left(\cot\theta_B \dfrac{\partial}{\partial x} + \dfrac{\partial}{\partial z}\right) E_0(\eta; x, z) = i a_0 E_0(\eta; x, z) \\ \qquad\qquad + i a_{\bar h} E_h(\eta; x, z), \\ \left(\cot\theta_B \dfrac{\partial}{\partial x} - \dfrac{\partial}{\partial z}\right) E_h(\eta; x, z) = i(a_0 + \eta) E_h(\eta; x, z) \\ \qquad\qquad + i a_h E_0(\eta; x, z), \end{cases} \tag{1}$$

where $E_{0,h}(\eta; x, z)$ are the complex amplitudes of the transmitted and reflected electric field waves, respectively, $\eta = 4\pi\cos\theta_B\,\omega/\lambda$ is the angular parameter used in the double-crystal diffraction in the ω–2θ mode, $a_0 = \pi\chi_0/(\lambda\gamma_0)$, $a_{h,\bar h} = C\pi\chi_{h,\bar h}/(\lambda\gamma_{h,0})$, λ is the X-ray wavelength in a vacuum, $\gamma_{0,h} = \sin\theta_B$, C is the polarization factor, and $\chi_g = -r_0\lambda^2 F_g/(\pi V_c)$ are the Fourier components of polarizability, with $g = 0$, h, $\bar h$. Here V_c is the volume of the unit cell, $r_0 = e^2/(mc^2)$ is the classical electron radius, e and m are the electric charge and mass of an electron, c is the speed of light, and F_g is the structure factor. More information about Takagi's equations and approximations used in them is given by Authier (2001) and Härtwig (2001).

Equation (1) can be simplified if both the incident plane wave and the crystal are homogeneous in the $\mathbf{x}$ direction, in which case there is no dependency on the x coordinate:

$$\begin{cases} \dfrac{\partial}{\partial z} E_0(\eta; z) = i a_0 E_0(\eta; z) + i a_{\bar h} E_h(\eta; z), \\ -\dfrac{\partial}{\partial z} E_h(\eta; z) = i(a_0 + \eta) E_h(\eta; z) + i a_h E_0(\eta; z), \end{cases} \tag{2}$$

which solution is well known in the case of Bragg geometry for an ideal crystal of thickness l_z (see *e.g.* Punegov, 1993; Punegov *et al.*, 2010). Taking into account the boundary conditions at the top $[E_0(\eta; z = 0) = 1]$ and the bottom $[E_h(\eta; z = l_z) = 0]$ surfaces of the crystal, the amplitude transmission coefficient $T(\eta) = E_0(\eta; z = l_z)$ and the amplitude reflection coefficient $R(\eta) = E_h(\eta; z = 0)$ are as follows:

$$T(\eta) = \exp[i(a_0 + \xi_1)l_z](\xi/Q), \tag{3}$$

$$R(\eta) = a_h\,[\exp(i\xi l_z) - 1]/Q, \tag{4}$$

where $\xi = (\psi^2 - 4a_h a_{\bar h})^{1/2}$, $\xi_{1,2} = (-\psi \pm \xi)/2$, $Q = \xi_1\exp(i\xi l_z) - \xi_2$ and $\psi = \eta + 2a_0$.

However, if the incident wave is transversely restricted, then one cannot use equation (2) and has to employ the more

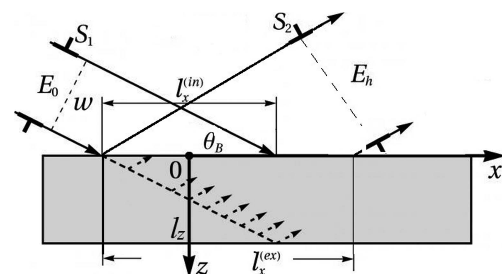

Figure 2
A diffraction scheme for the case of dynamical diffraction by a crystal of thickness l_z when the incident and the diffracted waves are transversely limited by slits S_1 and S_2, respectively.

general equation (1), because the wave amplitudes will be functions of the x coordinate.

We will use the following definitions of the inverse and direct Fourier transforms:

$$E_{0,h}(\eta; x, z) = \frac{1}{2\pi} \int_{-\infty}^{+\infty} \mathrm{d}\kappa \exp(i\kappa x) \hat{E}_{0,h}(\kappa, \eta; z), \tag{5}$$

$$\hat{E}_{0,h}(\kappa, \eta; z) = \int_{-\infty}^{+\infty} \mathrm{d}x \exp(-i\kappa x) E_{0,h}(\eta; x, z), \tag{6}$$

where κ is the coordinate in Fourier space which corresponds to the x coordinate in real space. If we substitute equations (5) and (6) into equation (1), we obtain

$$\begin{cases} \dfrac{\partial \hat{E}_0(\kappa, \eta; z)}{\partial z} = i(a_0 - \kappa \cot\theta_{\rm B}) \hat{E}_0(\kappa, \eta; z) + i a_{\bar{h}} \hat{E}_h(\kappa, \eta; z), \\ -\dfrac{\partial \hat{E}_h(\kappa, \eta; z)}{\partial z} = i(a_0 + \eta - \kappa \cot\theta_{\rm B}) \hat{E}_h(\kappa, \eta; z) \\ \qquad + i a_h \hat{E}_0(\kappa, \eta; z). \end{cases} \tag{7}$$

Fourier transforms of the wave amplitudes in equation (7) allows us to transform the two-dimensional system of equations (1) to the one-dimensional system of equations (7) in real space, which has analytical solutions. Note that the structure of equation (7) is similar to that of equation (2), exclusive of different coefficients.

To solve equations (7) we need to define their boundary conditions. Let us assume that the amplitude of the restricted incident wave at the top crystal surface is defined by

$$f(x, l_x^{(\rm in)}) = \begin{cases} 1 & -l_x^{(\rm in)}/2 \le x \le l_x^{(\rm in)}/2, \\ 0 & \text{otherwise.} \end{cases} \tag{8}$$

This function is shown in Fig. 3(*a*), where $l_x^{(\rm in)}$ is 300 and 900 µm. The function $f(x, l_x^{(\rm in)})$ can be also represented as a Fourier integral:

$$f(x, l_x^{(\rm in)}) = \frac{1}{2\pi} \int_{-\infty}^{\infty} \hat{f}(\kappa, l_x^{(\rm in)}) \exp(i\kappa x)\, \mathrm{d}\kappa. \tag{9}$$

In Fourier space this function has the following analytical expression:

$$\hat{f}\big(\kappa, l_x^{(\rm in)}\big) = \frac{\sin(\kappa\, l_x^{(\rm in)}/2)}{\kappa/2}. \tag{10}$$

The function $\hat{f}(\kappa, l_x^{(\rm in)})$ for 300 and 900 µm widths of the incident beam on the crystal surface is shown in Fig. 3(*b*).

If the amplitude of the incident wave at the crystal surface is described by equation (8), this corresponds to the following boundary condition in real space: $E_0(\eta; x, 0) = f(x, l_x^{(\rm in)})$. Using equations (6) and (10), we can also define the boundary condition for the mixed representation $\hat{E}_0(\kappa, \eta;\ 0) = \hat{f}(\kappa, l_x^{(\rm in)})$ at the top crystal surface ($z = 0$). The boundary condition for the diffracted wave (in the mixed representation) at the bottom surface of the crystal ($z = l_z$) is $\hat{E}_h(\kappa, \eta; l_z) = 0$.

Using these boundary conditions, we can write down analytical solutions to the system of equations (7) in the mixed (in real and Fourier space coordinates) form for $0 < z < l_z$:

$$\begin{aligned} \hat{E}_0(\kappa, \eta; z) &= \frac{\tilde{\xi}_1 \exp(i\tilde{\xi} l_z) - \tilde{\xi}_2 \exp(i\tilde{\xi} z)}{\tilde{Q}} \hat{f}(\kappa, l_x^{(\rm in)}) \\ &\quad \times \exp[i(\sigma_0 + \tilde{\xi}_2) z], \\ \hat{E}_h(\kappa, \eta; z) &= a_h \frac{\exp(i\tilde{\xi} l_z) - \exp(i\tilde{\xi} z)}{\tilde{Q}} \hat{f}(\kappa, l_x^{(\rm in)}) \\ &\quad \times \exp[i(\sigma_0 + \tilde{\xi}_2) z], \end{aligned} \tag{11}$$

where $\sigma_0 = (a_0 - \kappa \cot\theta_{\rm B})$, $\tilde{Q} = \tilde{\xi}_1 \exp(i\tilde{\xi} l_z) - \tilde{\xi}_2$, $\tilde{\xi}_{1,2} = (-\tilde{\psi} \pm \tilde{\xi})/2$, $\tilde{\xi} = (\tilde{\psi}^2 - 4 a_h a_{\bar{h}})^{1/2}$ and $\tilde{\psi} = \eta + 2a_0 - 2\kappa \cot\theta_{\rm B}$.

This mixed form solution (11) can be used to obtain [after substitution into equation (5)] the amplitudes of the reflected and transmitted waves as functions of the x and z coordinates and the angular parameter η:

$$\begin{aligned} E_0(\eta; x, z) &= \frac{1}{2\pi} \int_{-\infty}^{+\infty} \mathrm{d}\kappa\, \frac{\tilde{\xi}_1 \exp(i\tilde{\xi}\, l_z) - \tilde{\xi}_2 \exp(i\tilde{\xi} z)}{\tilde{Q}} \hat{f}(\kappa, l_x^{(\rm in)}) \\ &\quad \times \exp\{i[(\sigma_0 + \tilde{\xi}_2) z + \kappa x]\}, \end{aligned} \tag{12}$$

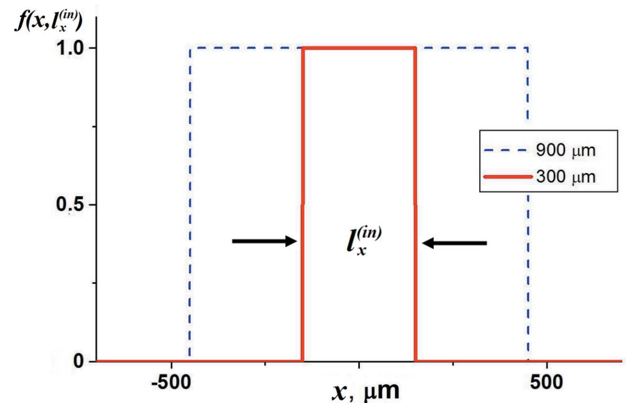

(*a*)

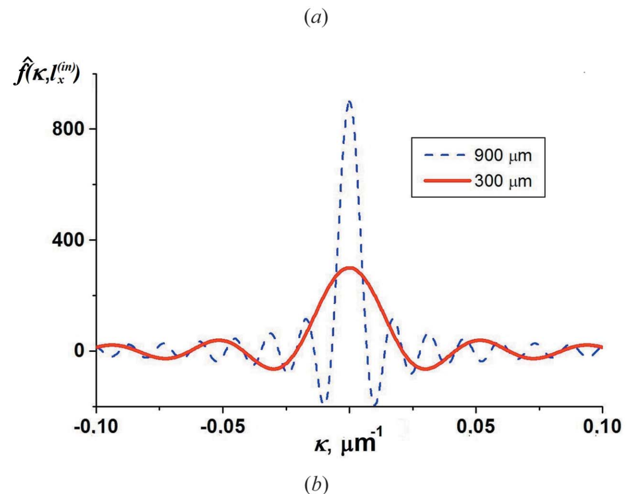

(*b*)

Figure 3
The boundary functions in direct (*a*) and Fourier (*b*) space for 300 and 900 µm wave width on the top crystal surface.

$$E_h(\eta; x, z) = \frac{a_h}{2\pi} \int_{-\infty}^{+\infty} \mathrm{d}\kappa \frac{\exp(i\tilde{\xi}\, l_z) - \exp(i\tilde{\xi}\, z)}{\tilde{Q}} \hat{f}(\kappa, l_x^{(\mathrm{in})}) \times \exp\{i[(\sigma_0 + \tilde{\xi}_2)z + \kappa x]\}. \quad (13)$$

These integral solutions (12) and (13) to Takagi's equations (1) were obtained for particular boundary conditions (8) and (10).

At the bottom of the crystal ($z = l_z$) the amplitude of the transmitted wave can be obtained from equation (12) as a function of the x coordinate and the angular parameter η:

$$T(\eta; x) = \frac{1}{2\pi} \int_{-\infty}^{+\infty} \mathrm{d}\kappa \frac{\tilde{\xi}}{\tilde{Q}} \hat{f}(\kappa, l_x^{(\mathrm{in})}) \exp\{i[(\sigma_0 + \tilde{\xi}_1) l_z + \kappa x]\}. \quad (14)$$

By substituting $z = 0$ in equation (13) we obtain the amplitude of the reflected wave at the top surface of the crystal:

$$R(\eta; x) = \frac{a_h}{2\pi} \int_{-\infty}^{+\infty} \mathrm{d}\kappa \frac{\exp(i\tilde{\xi} l_z) - 1}{\tilde{Q}} \hat{f}(\kappa, l_x^{(\mathrm{in})}) \exp(i\kappa x). \quad (15)$$

The wider the incident X-ray wave, the narrower the function $\hat{f}(\kappa, l_x^{(\mathrm{in})})$ is in Fourier space (Fig. 3). In the case of the incident plane wave the function $\hat{f}(\kappa, l_x^{(\mathrm{in})})$ transforms into the Dirac delta function [see equations 21.9-18c and 21.9-11 of Korn & Korn (1968) and also Wei *et al.* (2002)]:

$$\lim_{l_x^{(\mathrm{in})} \to \infty} \hat{f}\left(\kappa, l_x^{(\mathrm{in})}\right) = \lim_{l_x^{(\mathrm{in})} \to \infty} \frac{\sin(\kappa l_x^{(\mathrm{in})}/2)}{\kappa/2} = 2\pi\delta(\kappa). \quad (16)$$

Then, in the case of the plane incident wave [see equation (16)], solutions (14) and (15) transform into the well known amplitude transmission [equation (3)] and reflection [equation (4)] coefficients, respectively.

3. Reflection and transmission X-ray intensity distribution maps inside a crystal

Let us consider an incident plane monochromatic X-ray wave having σ polarization and unit intensity. This wave illuminates a crystal, and the angle between the wavevector of the incident wave and the X axis is $\theta_0 = \theta_\mathrm{B} + \omega_0$. Then the transmitted $I_\mathrm{T}(\eta_0; x, z)$ and reflected $I_\mathrm{R}(\eta_0; x, z)$ intensities inside the crystal are defined as follows:

$$I_\mathrm{T}(\eta_0; x, z) = |E_0(\eta_0; x, z)|^2, \quad I_\mathrm{R}(\eta_0; x, z) = |E_h(\eta_0; x, z)|^2, \quad (17)$$

where the amplitudes $E_{0,h}(\eta_0; x, z)$ are given in equations (12) and (13), $\eta_0 = 4\pi \cos\theta_\mathrm{B}\, \omega_0/\lambda$, and $\omega = \omega_0$ is a small deviation from the exact Bragg angle.

The numerical modelling is performed for a transversely restricted X-ray wave having the wavelength $\lambda = 0.154056$ nm (Cu $K\alpha_1$ radiation) in the case of an Si(111) reflection. The angular position was corrected on the refraction shift proportional to the real component of a_0 in equation (1). The Fourier components of polarizability, χ_g, where, $g = 0, h, \overline{h}$, were obtained from Sergey Stepanov's *X-Ray Server* (Stepanov & Forrest, 2008). The primary Bragg extinction length (Authier, 2001) for the Si(111) reflection is $l_{\mathrm{ext}}^{(z)} = \lambda|\sin\theta_\mathrm{B}|/(C\pi|\chi_h|)$ = 1.51 µm. The Bragg angle for this reflection is 14.221° and the interplanar distance $d_{111} = 3.1355$ Å. The thickness of the crystal is l_z = 100 µm.

Fig. 4 shows the reflection and transmission X-ray intensity distribution maps at different θ_0 inside a crystal for $l_x^{(\mathrm{in})}$ = 300 µm. These maps were calculated using equations (12), (13) and (17). The contours of equal intensity are shown on a logarithmic scale with a step size of 0.58 for intensity. Note that, although the thickness of the silicon crystal is 100 µm, Fig. 4 shows only the upper part of the crystal, for the z coordinate varying from 0 to 5 µm. At the larger depth both the transmitted and reflected intensities become negligible (in the vicinity of the Bragg diffraction angle) owing to primary extinction effects (Authier, 2001).

If the angle of incidence is exactly the Bragg angle (*i.e.* $\eta_0 = \omega_0 = 0$, $\theta_0 = \theta_\mathrm{B}$), then the intensity of the transmitted and reflected waves exponentially decreases with the crystal depth: $I_{\mathrm{T,R}}(0; x, z) \propto \exp(-2z/l_{\mathrm{ext}}^{(z)})$ (Authier, 2001) due to primary extinction. Some intensity oscillations are observed on the left side of the transmission and reflection intensity distribution maps in Figs. 4(*a*) and 4(*b*). There the area of the maximum transmitted intensity corresponds to the area of the minimum reflected intensity. These oscillations can be described as pseudo-*Pendellösung* oscillations, well known for the Laue diffraction case (Authier, 2001). Evidently, the transverse limitation of the incident beam shapes the area of the crystal where the diffraction occurs.

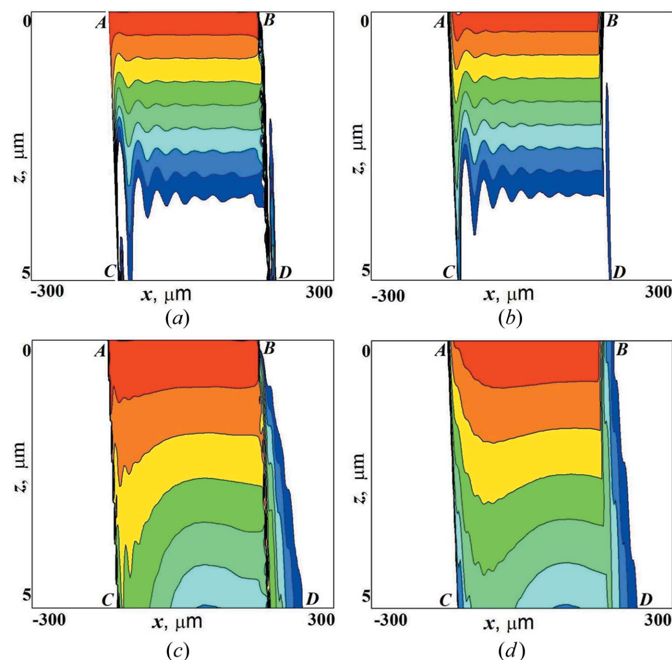

Figure 4
The transmission (*a*), (*c*) and reflection (*b*), (*d*) X-ray intensity distribution maps (on a logarithmic scale with a step size of 0.58 for intensity, where red and blue correspond to the highest and lowest intensity, respectively) at ω_0 = 0 (*a*), (*b*) and ω_0 = 0.3″ (*c*), (*d*) inside a crystal for the case of the illuminated area $l_x^{(\mathrm{in})}$ = 300 µm.

To the left of the line AC (Fig. 5) the lattice planes do not participate in the X-ray diffraction. Therefore, the scattering crystal volume is limited by the top surface ABY and bottom surface CDY planes as well as by the ACY plane. Consequently, along the line AC, for example, at the point L (see Fig. 5, where T is the transmitted wave and R is the reflected wave), the X-ray wave is incident to the scattering atomic planes in Laue geometry.

Note that the intensity of the transmitted wave decreases with depth (*i.e.* in the positive **z** direction) owing to primary extinction. The period of the pseudo-*Pendellösung* oscillations (in the **x** direction) is $l_{\rm ext}^{(x)} = \lambda|\cos\theta_{\rm B}|/(C|\chi_h|) = \pi\, l_{\rm ext}^{(z)}\cot\theta_{\rm B}$. Bushuev (1998) introduced a longitudinal extinction length $\Lambda_x = l_{\rm ext}^{(z)}\cot\theta_{\rm B}$, which differs only by a coefficient π from the period of the pseudo-*Pendellösung* oscillations shown above.

Moving to the right from the line AC in the positive **x** direction, X-ray diffraction predominantly transfers into the Bragg diffraction case, and, hence, the amplitude of the pseudo-*Pendellösung* oscillations reduces (Fig. 4). This physical phenomenon resembles the Bragg–Laue diffraction case in lateral (having a finite length in the lateral direction) crystals (Punegov *et al.*, 2016).

For the angular deviation $\omega_0 = 0.3''$ (Figs. 4*c* and 4*d*) the extinction length increases, while the intensity of the transmitted and reflected waves now decreases with the depth more slowly: $I_{\rm T,R}(\eta_0; x, z) \propto \exp[-2z(1-\eta_0^2/4a_h a_{\bar h})^{1/2}/l_{\rm ext}^{(z)}]$.

Whereas the left boundary (AC) of the transmitted and reflected waves is well defined, the right boundary (near the BD line) is more blurred owing to the dynamic interaction of X-ray waves inside the crystal (Fig. 4). This effect becomes more evident with the increase of the angular deviation from the exact Bragg condition (Figs. 4*c* and 4*d*), which is consistent with the conclusions of Berenson (1989).

Thus, a transversely limited incident X-ray wave 'cuts' in a plane parallel crystal slab a laterally limited volume with a cross section shaped as a parallelogram, the right-hand side of which is diffused.

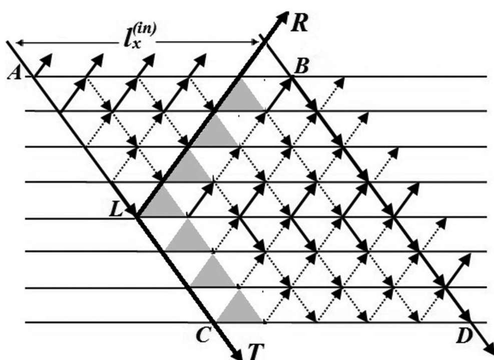

Figure 5
A schematic representation of dynamical diffraction of the spatially limited X-ray wave inside a crystal. Here T is the transmitted wave and R is the reflected wave. AB and CD are the top and bottom surfaces, respectively. AC defines a boundary of the incident wave.

4. The triple-crystal diffraction scheme

The triple-crystal X-ray diffraction scheme allows one to register two-dimensional maps of the diffracted intensity distribution in reciprocal space. These two-dimensional maps are dependent on two angular parameters, ω and ε, which specify the angular positions of the investigated sample and the analyser crystal (Iida & Kohra, 1979), respectively. In the symmetrical Bragg geometry these two angular parameters are related to the projections $q_{x,y}$ of the deviation of the diffraction vector from the reciprocal lattice point:

$$\begin{aligned} q_x &= k\sin\theta_{\rm B}(2\omega-\varepsilon),\\ q_z &= -k\cos\theta_{\rm B}\,\varepsilon, \end{aligned} \tag{18}$$

where $k = 2\pi/\lambda$. In the case of the triple-crystal diffraction scheme [the detailed geometry of this scheme is shown by Nesterets & Punegov (2000)] the angular variable η can be written as

$$\eta = q_x\cot\theta_{\rm B} - q_z. \tag{19}$$

To proceed from the double-crystal to the triple-crystal diffraction scheme in the case of spatially restricted waves, the amplitudes $E_{0,h}(\eta; x, z)$ in equations (12) and (13) must be Fourier transformed with respect to the q_x variable. Then, the intensity of the reflected X-ray wave at the top surface of the crystal is written as

$$I_{\rm R}(q_x, q_z) = \left|\frac{1}{l_{\rm norm}}\int\limits_{-l_x^{\rm (ex)}/2}^{l_x^{\rm (ex)}/2} {\rm d}x\,\exp(-iq_x x)E_h(\eta; x, 0)\right|^2. \tag{20}$$

In equation (20) we took into account that the X-ray wave reflected by the sample is incident on the analyser crystal (or a two-dimensional detector) as a transversely restricted wave with a lateral width of $l_x^{\rm (ex)}$. After some algebra, equation (20) can be represented in the following (cross-correlation) form:

$$I_{\rm R}(q_x, q_z) = \left|\frac{a_h}{2\pi\, l_{\rm norm}}\int\limits_{-\infty}^{+\infty}\frac{\exp(i\tilde\xi l_z)-1}{\tilde Q}\hat f(\kappa, l_x^{\rm (in)})\hat f(\kappa-q_x, l_x^{\rm (ex)})\,{\rm d}\kappa\right|^2. \tag{21}$$

Here $l_{\rm norm}$ is equal to the smaller of $l_x^{\rm (in)}$ and $l_x^{\rm (ex)}$; $\tilde\xi = (\tilde\psi^2 - 4a_h a_{\bar h})^{1/2}$, $\tilde\psi = 2a_0 - q_z + (q_x - 2\kappa)\cot\theta_{\rm B}$ and $\hat f(\kappa - q_x, l_x^{\rm (ex)}) = \sin[(\kappa-q_x)\,l_x^{\rm (ex)}/2]/[(\kappa-q_x)/2]$.

Now we consider some special cases.

4.1. Unrestricted reflected X-ray wave (absence of slit S_2)

Consider the case where slit S_2 is absent, and the analyser crystal and detector collect the entire reflected wave. Mathematically, this means that $l_x^{\rm (ex)} \to \infty$. Then, the function $\hat f(\kappa - q_x, l_x^{\rm (ex)}) = 2\pi\delta(\kappa - q_x)$, which can be substituted into equation (21) to obtain the solution for the reflected wave intensity distribution in reciprocal space:

$$I_{\rm R}(q_x, q_z) = \left| a_h \frac{\exp(i\overline{\xi} l_z) - 1}{\overline{Q}} {\rm sinc}(q_x l_x^{(\rm in)}/2) \right|^2, \qquad (22)$$

where $\overline{\xi} = (\overline{\psi}^2 - 4a_h a_{\overline{h}})^{1/2}$, $\overline{\xi}_{1,2} = (-\overline{\psi} \pm \overline{\xi})/2$, $\overline{Q} = \overline{\xi}_1 \exp(i\overline{\xi} l_z) - \overline{\xi}_2$, $\overline{\psi} = 2a_0 - q_x \cot\theta_{\rm B} - q_z$ and ${\rm sinc}(x) = \sin(x)/x$.

Note that in the expression for $\overline{\psi}$ the term $q_x \cot\theta_{\rm B}$ is taken with a minus sign. The intensity in equation (22) depends on the lateral size $l_x^{(\rm in)}$ of the incident X ray wave. In the case of an ω–2θ scan (an analogy of the double-crystal diffraction scheme) the result shown in equation (22) coincides with the conclusions of Bushuev (1998) and Bushuev & Oreshko (2007) obtained for the double-crystal diffraction scheme.

Fig. 6 demonstrates how the reciprocal space maps (RSMs) near the Si(111) reciprocal lattice vector depend (in the absence of slit S_2) on the lateral width, $l_x^{(\rm in)}$, of the incident X-ray wave, defined by slit S_1. In the case of a wide ($l_x^{(\rm in)} = 900$ µm) incident beam, an inclined oscillating streak, related to the width of the incident beam, and a narrow vertical streak of the so-called main peak (see Fig. 6*a*) appear on the RSM. The angle between the main streak and the oscillating streak is equal to the Bragg angle. In the triple-crystal diffraction scheme this oscillating streak is usually called the analyser pseudo-peak. The length and width of this inclined oscillating streak increase while the lateral width of the incident wave decreases (Fig. 6*b* and 6*c*).

4.2. Unrestricted incident plane wave (absence of slit S_1)

Consider the case when a laterally unrestricted plane X-ray wave is incident on the top surface of the crystal. This means that $l_x^{(\rm in)} \to \infty$ and, as shown above [see equation (16)], $\hat{f}(\kappa, l_x^{(\rm in)}) = 2\pi\delta(\kappa)$, which can be substituted into equation (21):

$$I_{\rm R}(q_x, q_z) = \left| a_h \frac{\exp(i\overline{\xi} l_z) - 1}{\overline{Q}} {\rm sinc}(q_x l_x^{(\rm ex)}/2) \right|^2, \qquad (23)$$

where $\overline{\xi} = (\overline{\psi}^2 - 4a_h a_{\overline{h}})^{1/2}$, $\overline{\xi}_{1,2} = (-\overline{\psi} \pm \overline{\xi})/2$, $\overline{Q} = \overline{\xi}_1 \exp(i\overline{\xi} l_z) - \overline{\xi}_2$ and $\overline{\psi} = 2a_0 + q_x \cot\theta_{\rm B} - q_z$.

Equation (23) demonstrates that the intensity of the reflected (scattered) wave depends on the lateral width $l_x^{(\rm ex)}$. In addition, the term $q_x \cot\theta_{\rm B}$, present in equation (23) through the angular parameter $\overline{\psi}$, has a positive sign in contrast to equation (22). Also note that expressions (22) and (23) have a very similar form. The difference is only in parameters $l_x^{(\rm in)} \leftrightarrow l_x^{(\rm ex)}$ in the sinc function and $-q_x \cot\theta_{\rm B} \leftrightarrow q_x \cot\theta_{\rm B}$ in $\overline{\psi}$.

Fig. 7 demonstrates the calculated RSMs for the laterally unrestricted incident X-ray wave while the lateral size of the reflected wave is either 900 or 300 or 30 µm. Comparison of Figs. 6 and 7 shows that the RSMs for the same size of the incident and reflected beams have a mirror symmetry with respect to the vertical axis. This directly follows from

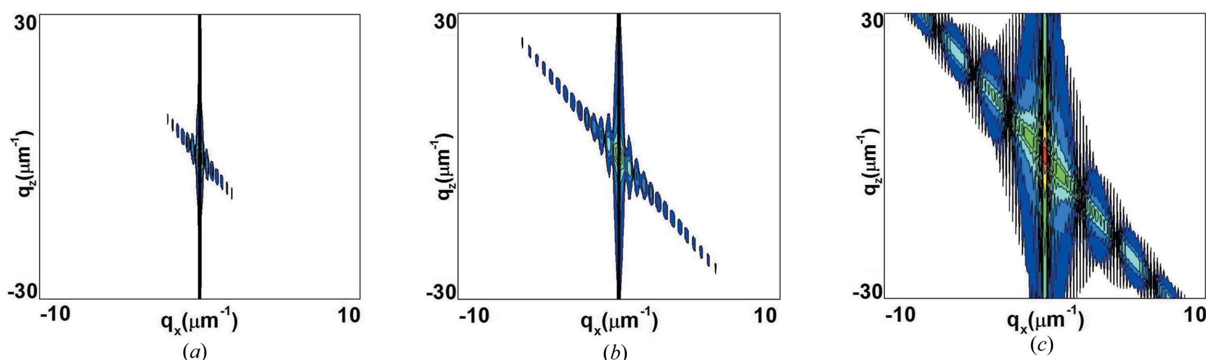

Figure 6
Calculated RSMs (on a logarithmic scale with a step size of 0.18 for intensity, where red and blue correspond to the highest and lowest intensity, respectively) near the Si(111) reciprocal space vector for different lateral widths, $l_x^{(\rm in)}$, of the incident wave: (*a*) 900 µm, (*b*) 300 µm, (*c*) 30 µm. The lateral width of the reflected wave is unrestricted.

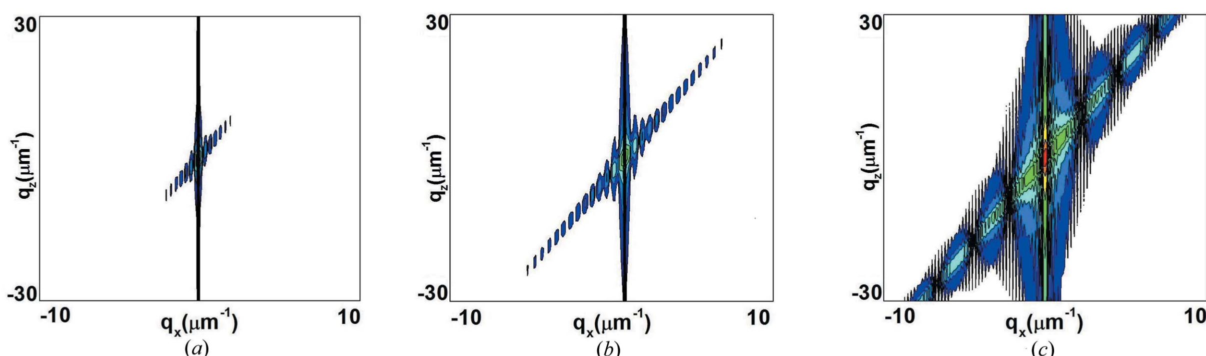

Figure 7
Calculated RSMs (on a logarithmic scale with a step size of 0.18 for intensity, where red and blue correspond to the highest and lowest intensity, respectively) near the Si(111) reciprocal space vector for different lateral widths, $l_x^{(\rm ex)}$, of the reflected wave: (*a*) 900 µm, (*b*) 300 µm, (*c*) 30 µm. The width of the incident wave is unrestricted.

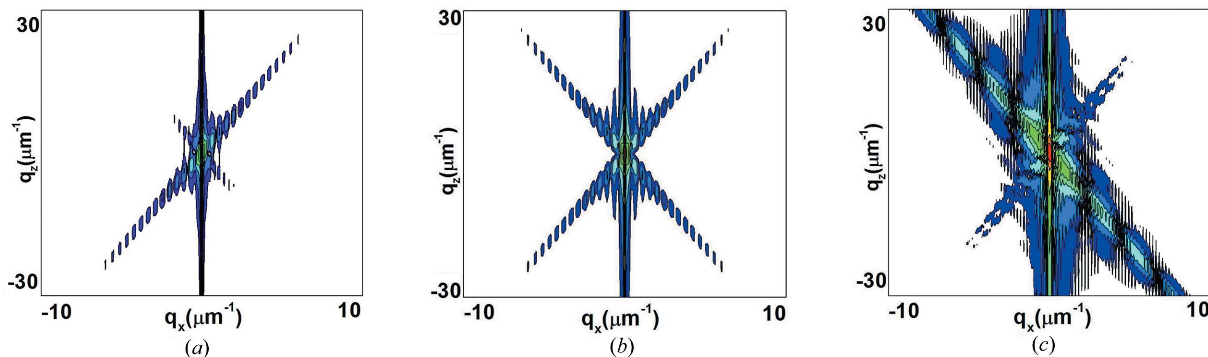

Figure 8
Calculated RSMs (on a logarithmic scale with a step size of 0.18 for intensity, where red and blue correspond to the highest and lowest intensity, respectively) near the Si(111) reciprocal space vector for different lateral widths of the incident beam: (*a*) 900 µm, (*b*) 300 µm, (*c*) 30 µm. The lateral size of the reflected beam is 300 µm.

equations (22) and (23), where the terms $q_x \cot\theta_{\rm B}$ in the expressions for the angular parameter $\overline{\psi}$ have opposite signs.

If in equation (23) the lateral width of the reflected wave $l_x^{(\rm ex)} \to \infty$, then $\hat{f}(q_x, l_x^{(\rm ex)}) = 2\pi\delta(q_x)$ and the reflected wave intensity (in the case of unrestricted incident and reflected X-ray waves) is

$$I_{\rm R}(q_x, q_z) = \left| 2\pi\delta(q_x)\, a_h \frac{\exp(i\overline{\xi} l_z) - 1}{\overline{Q}} \right|^2. \qquad (24)$$

4.3. Formation of RSMs in the general case of the transversely restricted incident and reflected X-ray waves

In the general case when both the incident and reflected waves are transversely restricted (by slits S_1 and S_2), the RSMs can be calculated using equation (21), which provides a general solution for transversely restricted waves. Fig. 8 shows simulations of RSMs near the Si(111) reciprocal space vector for a crystal having a thickness l_z = 100 µm for three different lateral sizes of the incident wave, $l_x^{(\rm in)}$, namely 900, 300 and 30 µm, while the lateral size of the reflected wave, $l_x^{(\rm ex)}$ = 300 µm, is still unchanged.

If both waves (transmitted and reflected) are spatially restricted, a mirror symmetry of inclined streaks (with respect to the vertical axis) is observed in the RSMs. The length of these streaks depends on the size of slits S_1 and S_2: the narrower the slit, the wider and longer the intensity streak in the RSM. The direction of the streaks in reciprocal space coincides with the direction of the monochromator and analyser pseudo-peaks in the triple-crystal diffraction scheme. If the lateral dimensions of the incident and diffracted beams are equal, the RSM has a symmetrical shape (Fig. 8*b*). If one of the slits, for instance, S_1, is significantly narrower than the other slit, S_2, changes in the shape and size of the intensity streaks are evident (Fig. 8*c*).

4.4. Cross-sectional analysis of RSMs

First we consider the situation when slit S_2 is absent. Then the RSMs' cross sections can be calculated using equation (22), which may be represented as a product of two functions: $I_{\rm R}(q_x, q_z) = |R_1(q_x, q_z)\, R_2(q_x)|^2$, where $R_1(q_x, q_z) = a_h \times [\exp(i\overline{\xi} l_z) - 1]/\overline{Q}$ and $R_2(q_x) = \sin(q_x l_x^{(\rm in)}/2)/(q_x l_x^{(\rm in)}/2)$. The first function, $R_1(q_x, q_z)$, coincides (in its form) with the classical solution (4) and depends on the thickness of the crystal l_z. The second function, $R_2(q_x)$, which squared equals the Laue

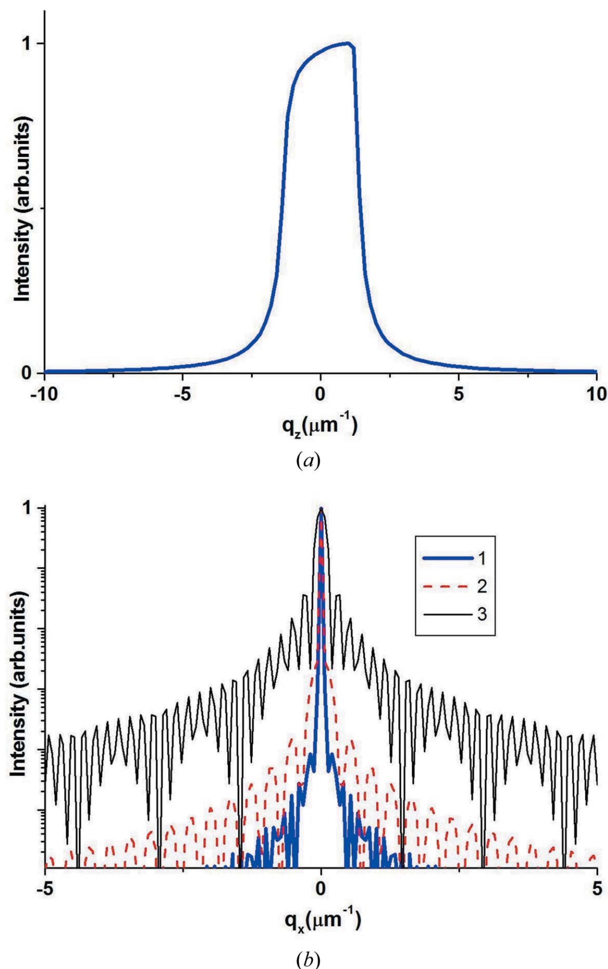

Figure 9
The calculated q_z (*a*) and q_x (*b*) (on a logarithmic scale) cross sections of the Si(111) RSMs for different lateral widths of the incident beam: (1) 900 µm, (2) 300 µm, (3) 30 µm.

interference function, is determined by the width of the top crystal surface illuminated by the incident X-ray wave.

Fig. 9 shows cross sections (along the q_x and q_z axes) of the simulated RSMs near a (111) reciprocal space vector of a perfect Si(111) crystal for three different lateral widths of the incident beam. The ω–2θ diffraction curves or, in other words, the q_z cross section of the RSMs at $q_x = 0$ for all three presented RSMs are identical and represent the Darwin curve (Fig. 9*a*). Thus, for a thick perfect crystal the lateral width of the incident beam does not affect the profile of the q_z cross section of the RSM. The rocking curves (ω curves) or, in other words, the q_x cross sections of Si(111) RSMs at $q_z = 0$ show dependency on the lateral width of the incident beam (see Fig. 9*b*): the smaller the lateral width of the incident beam, the wider the rocking curve.

Often the cross sections of experimental RSMs are presented as functions of the angular deviation, ω, from the exact Bragg position. In the ω–2θ scanning mode or in the q_z cross-sectional scan, when for all angular positions $\omega = \varepsilon/2$ (*i.e.* $q_x = 0$), one obtains that $\overline{\psi} = 2a_0 + 2k\cos\theta_{\rm B}\,\omega$. Taking into account that $R_2(q_x = 0) = 1$, the resulting expression for the reflected intensity is $I_{\rm R}(q_x = 0, \omega) = |a_h[\exp(i\overline{\xi}l_z) - 1]/\overline{Q}|^2$, where $\overline{\xi} = [(2a_0 + 2k\cos\theta_{\rm B}\,\omega)^2 - 4a_h a_{\overline{h}}]^{1/2}$. This expression shows that the cross section in the ω–2θ scanning mode does not depend on the lateral width of the incident X-ray beam.

Fig. 10(*a*) shows a Darwin curve in the vicinity of the 111 reflection for a 100 µm thick Si(111) perfect crystal as a function of the angular deviation ω. The full width at half-maximum (FWHM) of the diffraction curve is about 7″.

In the ω-scan mode ($q_z = 0$, $q_x = 2k\sin\theta_{\rm B}\,\omega$, $\overline{\psi} = 2a_0 - 2k\cos\theta_{\rm B}\,\omega$), the reflected intensity can be written as $I_{\rm R}(\omega, q_z = 0) = |R_1(\omega, q_z = 0)|^2\,[R_2(\omega)]^2$. Unlike the ω–2θ scan, the reflected intensity depends on the product of two functions. The first, $|R_1(\omega, q_z = 0)|^2 = |a_h[\exp(i\overline{\xi}l_z) - 1]/\overline{Q}|^2$, represents the ω–2θ diffraction curve, while the second one, $[R_2(\omega)]^2 = \{[\sin(k\sin\theta_{\rm B}\,\omega\, l_x^{\rm (in)})]/(k\sin\theta_{\rm B}\,\omega\, l_x^{\rm (in)})\}^2$, depends on the lateral width of the incident X-ray wave and is a narrow function of the angle ω (see Fig. 10*b*, curve 2), where $\overline{\xi} = [(2a_0 - 2k\cos\theta_{\rm B}\,\omega)^2 - 4a_h a_{\overline{h}}]^{1/2}$. Note that $|R_1(\omega, q_z = 0)|^2 = |R_1(q_x = 0, -\omega)|^2$, that is the ω scans of the Darwin curves for the vertical $[|R_1(q_x = 0, -\omega)|^2]$ and lateral $[|R_1(\omega, q_z = 0)|^2]$ cross sections of the RSMs are mirrored.

Fig. 10(*b*) shows an ω scan (blue curve 1) for a 100 µm thick Si crystal in the vicinity of the 111 reflection, where the lateral width of the incident X-ray beam $l_x^{\rm (in)} = 300$ µm. This ω rocking curve (blue curve, 1) is a product of the narrow Laue interference function (red curve, 2) and a broad Darwin curve (black curve, 3). Thus the narrow curve $[R_2(\omega)]^2$ determines the narrow shape of the ω scan, having an FWHM of less than 1″.

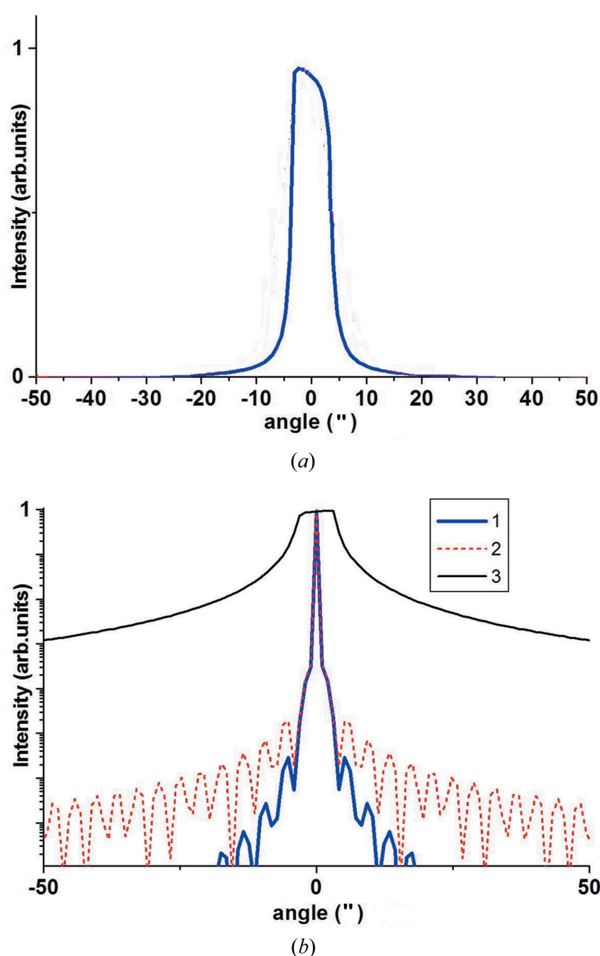

Figure 10
(*a*) The ω–2θ diffraction curve $I_{\rm R}(q_x = 0, \omega) = |R_1(q_x = 0, \omega)|^2$ in the vicinity of the 111 reflection for a 100 µm thick Si(111) crystal as a function of the angular parameter ω. (*b*) The blue curve 1 is the rocking curve $I_{\rm R}(\omega, 0) = |R_1(\omega)|^2\,[R_2(\omega)]^2$ for an incident X-ray beam with the lateral width $l_x^{\rm (in)} = 300$ µm; the red curve 2 is the function $[R_2(\omega)]^2$; the black curve 3 is the function $|R_1(\omega)|^2$ (the Darwin curve).

5. Instrumental function

To analyse real experimental data, the analytical results obtained in previous sections should be complemented by an instrumental function, which contains information about the monochromator and analyser crystals used in the experiment. There are numerous theoretical and experimental analyses of instrumental functions for different types of diffractometers (Zaumseil & Winter, 1982; Holý & Mikulík, 1996; Fewster, 1989; Gartstein *et al.*, 2001; Boulle *et al.*, 2002; Mikhalychev *et al.*, 2015). The first theoretical description of how different configurations of collimator/monochromator and analyser crystals in the triple-crystal diffractometer affect the registered intensity was published by Zaumseil & Winter (1982). Recent modelling of instrumental functions based on semi-analytical backward ray tracing for high-resolution X-ray diffractometers was reported by Mikhalychev *et al.* (2015). If the main X-ray optical elements (*e.g.* collimators/monochromators and analyser crystals) employ multiple reflections (Mikhalychev *et al.*, 2015), the intensity of the monochromator and analyser pseudo-peaks is significantly reduced and is sometimes totally suppressed (Fewster, 1989). Therefore, an investigation of the effects of the instrumental function on RSM distortions is essential for the correct interpretation of experimental RSMs.

In our analysis we suppose that the scattered intensity is already integrated along the q_y direction. In addition, we will also neglect non-monochromaticity of the incident radiation, because its impact is much smaller than that caused by the resolution functions of the monochromator and analyser crystals (Mikhalychev *et al.*, 2015). Let us now consider the angular distribution of the scattered intensity $I_R^{(ins)}(q_x, q_z)$ that is recorded in the triple-crystal diffraction scheme with slits S_1 and S_2, which spatially restrict the incident and the reflected waves, respectively.

In the case of symmetrical diffraction the angular deviation of the sample, ω, and the analyser crystal, ε, are connected with projections $q_{x,z}$ (Nesterets & Punegov, 2000):

$$\omega = \frac{q_x \cos\theta_B - q_z \sin\theta_B}{h \cos\theta_B}, \qquad \varepsilon = -\frac{q_z}{k \cos\theta_B}, \tag{25}$$

where $\mathbf{h}$ is the vector of the reciprocal lattice. In the experiment the angular deviation of the investigated sample, ω, is related to the angular deviation of the monochromator crystal by $\delta = -\omega$ and to the angular deviation of the analyser crystal by $\gamma = \omega - \varepsilon$. The appropriate reflection coefficients of the monochromator and analyser crystals are then $R^M(-\omega)$ and $R^A(\omega - \varepsilon)$, respectively.

Thus, the normalized diffracted intensity distribution in reciprocal space, corrected by the instrumental function, can be represented in the following form:

$$I_R^{(ins)}(q_x, q_z) = \frac{\int_{-\infty}^{+\infty}\int_{-\infty}^{+\infty} dq'_x\, dq'_z\, \overline{R}^M(q'_x, q'_z)\, \overline{R}^A(q'_x, q'_z)\, I_R(q_x - q'_x, q_z - q'_z)}{\int_{-\infty}^{+\infty}\int_{-\infty}^{+\infty} dq'_x\, dq'_z\, R^M(q'_x, q'_z)\, R^A(q'_x, q'_z)}, \tag{26}$$

where

$$\begin{aligned} \overline{R}^M(q'_x, q'_z) &= R^M\left(-\frac{q'_x \cos\theta_B - q'_z \sin\theta_B}{h\cos\theta_B}\right), \\ \overline{R}^A(q'_x, q'_z) &= R^A\left(\frac{q'_x \cos\theta_B - q'_z \sin\theta_B}{h\cos\theta_B} + \frac{q_z}{k\cos\theta_B}\right) \end{aligned} \tag{27}$$

are the reflection coefficients for the monochromator and analyser crystals, respectively; $I_R(q_x, q_z)$ is the scattering intensity, calculated using equation (22).

We can use for the functions $R^{M,A}(\omega) = |r(\omega)|^2$ the reflection coefficients for semi-infinite perfect crystals, where the amplitude reflection coefficient, $r(\omega)$, is the well known function (Authier, 2001)

$$r(\omega) = \begin{cases} a_h^{M,A}/\xi_1^{M,A}(\omega) & \text{if } \operatorname{Im}[\xi^{M,A}(\omega)] < 0, \\ a_h^{M,A}/\xi_2^{M,A}(\omega) & \text{if } \operatorname{Im}[\xi^{M,A}(\omega)] > 0. \end{cases} \tag{28}$$

The coefficients $\xi^{M,A}(\omega)$ and $\xi_{1,2}^{M,A}(\omega)$ depend on the parameters of the X-ray radiation, as well as on the structural

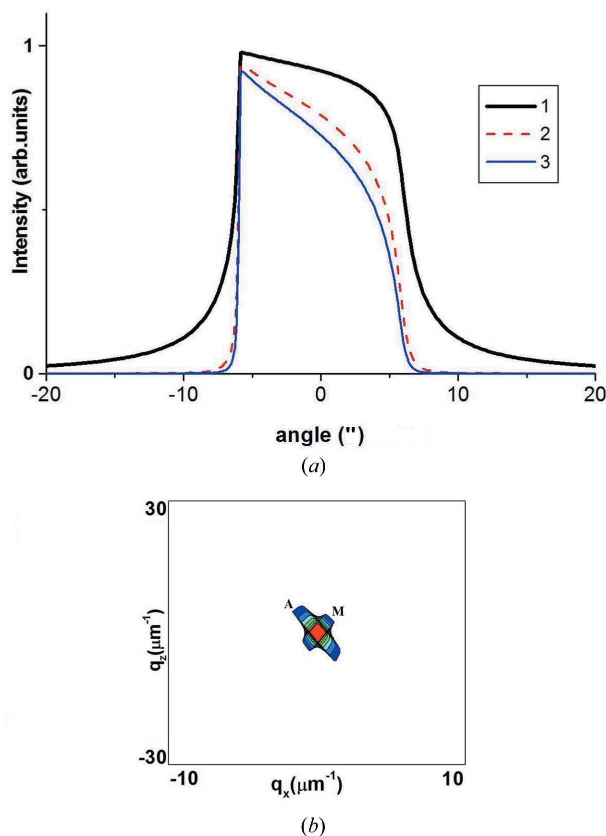

Figure 11
(*a*) Rocking curves for the Ge(220) collimator/monochromator crystal in the case of a single reflection (curve 1), a triple-bounce design (curve 2) and a four-bounce design (curve 3). (*b*) RSM (on a logarithmic scale with a step size of 0.18 for intensity, where red and blue correspond to the highest and lowest intensity, respectively) of the instrumental function for a four-bounce Ge(220) monochromator and a three-bounce Ge(220) analyser crystal. M and A are the monochromator and analyser pseudo-peaks, respectively.

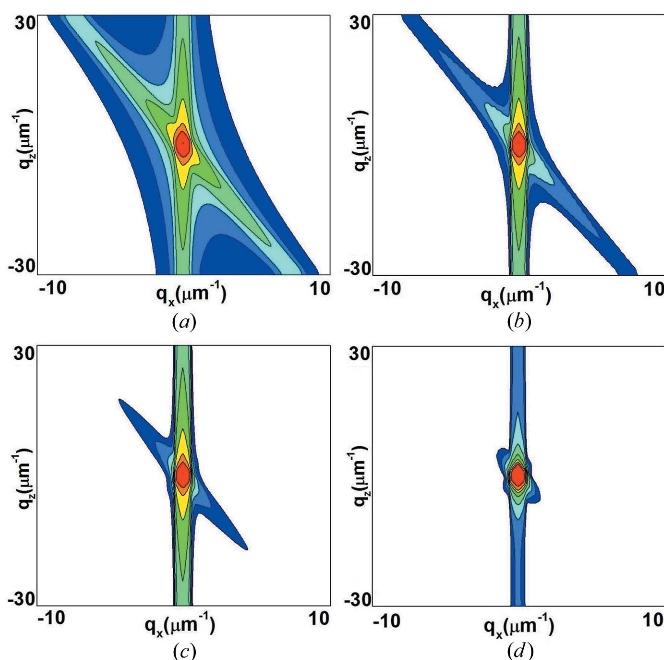

Figure 12
The simulated RSMs (on a logarithmic scale with a step size of 0.18 for intensity, where red and blue correspond to the highest and lowest intensity, respectively) with the impact of the instrumental function for different $l_x^{(in)}$: (*a*) 30 μm, (*b*) 300 μm, (*c*) 900 μm, (*d*) $l_x^{(in)} = \infty$.

parameters of the monochromator (M) and analyser (A) crystals: $\xi^{\rm M,A}(\omega) = [(2a_0^{\rm M,A} + \overline{\eta})^2 - 4a_h^{\rm M,A}a_{-h}^{\rm M,A}]^{1/2}$, $\xi_{1,2}^{\rm M,A}(\omega) = [-\overline{\eta} \pm \xi^{\rm M,A}(\omega)]/2$ and $\overline{\eta} = 4\pi\cos\theta_{\rm B}^{\rm M,A}\,\omega/\lambda$. Here ω is the angular deviation from the appropriate Bragg angular position, the coefficients $a_{0,h,\overline{h}}^{\rm M,A}$ are equivalent to the coefficients $a_{0,h,\overline{h}}$ in equation (1), and $\theta_{\rm B}^{\rm M,A}$ are the Bragg angles for the monochromator and the analyser crystals, respectively.

Using equation (26) we can analyse the impact of the instrumental function on the formation of RSMs. In our simulations we use a Ge(220) four-bounce monochromator crystal and a Ge(220) triple-bounce analyser crystal. The rocking curves for the Ge(220) triple-bounce and four-bounce crystals and the RSM of the instrumental function are shown in Fig. 11.

Fig. 12 shows RSMs, simulated with the impact of the instrumental function, for the different lateral sizes of the incident beam $l_x^{\rm (in)}$ on the top surface of the investigated crystal. Fig. 6 shows these RSMs simulated without the impact of the instrumental function. The small lateral size of the incident beam (Fig. 12*a*) causes a blurred intensity distribution in the RSM.

An increase of the lateral width of the X-ray illuminated area narrows the diffraction pattern (Figs. 12*b* and 12*c*). The inclined strips on the RSMs are the result of the superposition of two effects: the finite width of the incident beam (see Fig. 6) and the analyser pseudo-peak. The four-bounce monochromator pseudo-peak is practically non-observable on the RSMs.

Fig. 12(*d*) shows the RSM simulated with the impact of the instrumental function in the case of an indefinitely wide X-ray incident beam. Short streaks of the monochromator and analyser crystal pseudo-peaks are observed, due to the effect of the instrumental function. Without the instrumental function effects, only the main peak would be observable (Punegov *et al.*, 2016).

The q_x and q_z cross sections of RSMs calculated for the different $l_x^{\rm (in)}$ while accounting for the instrumental function are shown in Fig. 13.

The extent and intensity of the q_x cross-section 'tails' depend on the lateral width of the incident radiation: the wider the incident beam, the weaker the intensity of the 'tails'. In the case of the unrestricted plane incident wave the 'tails' are absent (Fig. 13*a*, curve 4). The instrumental function extends the q_z cross section and changes its shape [compare in Fig. 13(*b*) curves 1 and 2 and the Darwin curve 3). Unlike the q_x cross section, the width of the incident beam does not affect the shape of the q_z cross section, with hardly noticeable distinctions existing for the spatially unrestricted plane incident X-ray wave (Fig. 13*b*, curve 2).

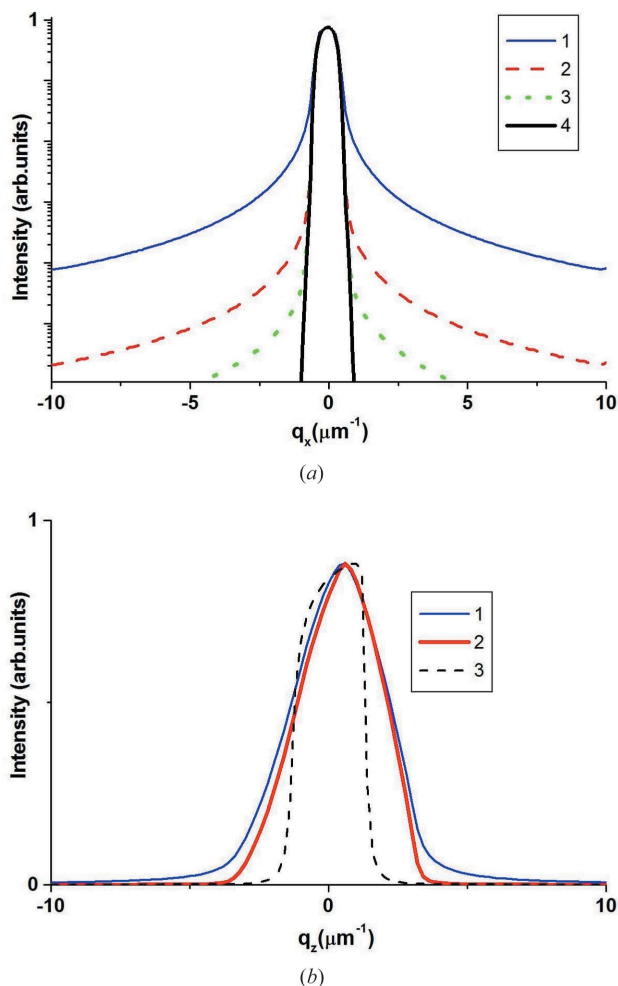

Figure 13
(*a*) Simulated q_x cross sections of RSMs with the impact of the instrumental function, with $l_x^{\rm (in)}$ of 30 µm (curve 1), 300 µm (curve 2), 900 µm (curve 3) and ∞ (curve 4). (*b*) Calculated q_z cross sections of RSMs with the impact of the instrumental function for $l_x^{\rm (in)}$ of 30 µm, 300 µm and 900 µm (curve 1, curves are indistinguishable); for $l_x^{\rm (in)} = \infty$ (curve 2); and for all $l_x^{\rm (in)}$ (curve 3, curves are indistinguishable) without taking into account the instrumental function.

6. Concluding remarks

The developed approach allows one to correctly simulate RSMs and their cross sections for perfect crystals. Up to the present only RSMs of diffuse scattering were usually simulated, because the coherent component was typically calculated as a δ function (Kaganer *et al.*, 1997) in the case of the laterally unrestricted incident plane wave. This prevented the quantitative analysis of both the coherent and diffuse scattering components. The developed approach will be applicable for X-ray or neutron optics as well as for the optics of photonic and liquid crystals. This approach will also be useful for coherent diffraction imaging techniques (Pavlov *et al.*, 2017).

It should be emphasized that the developed approach to the theory of dynamical X-ray diffraction is more general than the existing approaches because it takes into account the spatially restricted X-ray beams that are used in all real experiments. This approach may be developed further by extending the statistical dynamical diffraction theory to the case of the spatially restricted beams. This will allow one to correctly calculate intensities of the coherent and diffuse scattered waves.

Funding information

VIP and AVK acknowledge financial support from the Russian Foundation for Basic Research (projects No. 16-43-

110350, No. 17-02-00090) and the Ural branch of the Russian Academy of Sciences (project No. 15-9-1-13). KMP acknowledges financial support from the University of New England.

References

Authier, A. (2001). *Dynamical Theory of X-ray Diffraction.* Oxford University Press.
Berenson, R. (1989). *Phys. Rev. B*, **40**, 20–28.
Bhagavannarayana, G. & Zaumseil, P. (1997). *J. Appl. Phys.* **82**, 1172–1177.
Boulle, A., Masson, O., Guinebretière, R., Lecomte, A. & Dauger, A. (2002). *J. Appl. Cryst.* **35**, 606–614.
Bushuev, V. A. (1998). *Dynamical Diffraction of Bounded X-ray Beams.* Preprint of the Physics Department of Moscow State University, No. 14/1998, pp. 1–12.
Bushuev, V. A. & Oreshko, A. P. (2007). *J. Surf. Invest. X-ray Synchrotron Neutron Tech.* **1**, 21–27.
Faleev, N. N., Honsberg, C. & Punegov, V. I. (2013). *J. Appl. Phys.* **113**, 163506.
Fewster, P. F. (1989). *J. Appl. Cryst.* **22**, 64–69.
Gartstein, E., Mandelbrot, M. & Mogilyanski, D. (2001). *J. Phys. D Appl. Phys.* **34**, A57–A63.
Härtwig, J. (2001). *J. Phys. D Appl. Phys.* **34**, A70–A77.
Holý, V. & Mikulík, P. (1996). *X-ray and Neutron Dynamical Diffraction Theory and Applications*, NATO ASI Series, Vol. 357, edited by A. Authier, S. Lagomarsino & B. K. Tanner, pp. 259–268. New York: Plenum Press.
Iida, A. & Kohra, K. (1979). *Phys. Status Solidi (A)*, **51**, 533–542.
Irzhak, D. V., Knyasev, M. A., Punegov, V. I. & Roshchupkin, D. V. (2015). *J. Appl. Cryst.* **48**, 1159–1164.
Jergel, M., Mikulík, P., Majková, E., Luby, Š., Senderák, R., Pinčík, E., Brunel, M., Hudek, P., Kostič, I. & Konečníková, A. (1999). *J. Appl. Phys.* **85**, 1225–1227.
Kaganer, V. M., Köhler, R., Schmidbauer, M., Opitz, R. & Jenichen, B. (1997). *Phys. Rev. B*, **55**, 1793–1810.
Kazimirov, A. Yu., Kovalchuk, M. V. & Kohn, V. G. (1990). *Acta Cryst.* A**46**, 643–649.
Korn, G. A. & Korn, T. M. (1968). *Mathematical Handbook*. New York: McGraw Hill Book Company.
Lomov, A. A., Punegov, V. I., Nohavica, D., Chuev, M. A., Vasiliev, A. L. & Novikov, D. V. (2014). *J. Appl. Cryst.* **47**, 1614–1625.
Mikhalychev, A., Benediktovitch, A., Ulyanenkova, T. & Ulyanenkov, A. (2015). *J. Appl. Cryst.* **48**, 679–689.
Nesterets, Y. I. & Punegov, V. I. (2000). *Acta Cryst.* A**56**, 540–548.
Pavlov, K. M., Punegov, V. I., Morgan, K. S., Schmalz, G. & Paganin, D. M. (2017). *Sci. Rep.* **7**, 1132.
Punegov, V. I. (1993). *Phys. Status Solidi (A)*, **136**, 9–19.
Punegov, V. I. (2012). *Tech. Phys.* **57**, 37–43.
Punegov, V. I. (2015). *Physics-Uspekhi*, **58**, 419–445.
Punegov, V. I., Kolosov, S. I. & Pavlov, K. M. (2014). *Acta Cryst.* A**70**, 64–71.
Punegov, V. I., Kolosov, S. I. & Pavlov, K. M. (2016). *J. Appl. Cryst.* **49**, 1190–1202.
Punegov, V. I., Nesterets, Y. I. & Roshchupkin, D. V. (2010). *J. Appl. Cryst.* **43**, 520–530.
Stepanov, S. & Forrest, R. (2008). *J. Appl. Cryst.* **41**, 958–962.
Takagi, S. (1962). *Acta Cryst.* **15**, 1311–1312.
Wei, G. W., Zhao, Y. B. & Xiang, Y. (2002). *Int. J. Numer. Methods Eng.* **55**, 913–946.
Zaumseil, P. & Winter, U. (1982). *Phys. Status Solidi (A)*, **70**, 497–505.